

advances.sciencemag.org/cgi/content/full/6/46/eabd3556/DC1

Supplementary Materials for

Magnetic resonance imaging of spin-wave transport and interference in a magnetic insulator

Iacopo Bertelli, Joris J. Carmiggelt, Tao Yu, Brecht G. Simon, Coosje C. Pothoven, Gerrit E. W. Bauer, Yaroslav M. Blanter, Jan Aarts, Toeno van der Sar*

*Corresponding author. Email: t.vandersar@tudelft.nl

Published 11 November 2020, *Sci. Adv.* **6**, eabd3556 (2020)
DOI: 10.1126/sciadv.abd3556

This PDF file includes:

Supplementary Text
Sections S1 to S3
Figs. S1 to S9
References

Supplementary Text

Section S1: Determination of the NV-YIG distance

The distance x_0 between the YIG surface and the NV sensing layer is an important parameter for the reconstruction of spin-wave amplitude from the detected field (Fig. 2 of the main text). We determined x_0 by sending a DC current I_{DC} through the stripline and characterizing the resulting magnetic field $\mathbf{B}_{DC}(x_0, y)$ using the NV sensing layer. This field causes spatially dependent shifts in the NV ESR frequencies (Fig. S1 A-B) from which we can extract x_0 as described next. Considering an infinitely thin stripline of width w with its center at $x = y = 0$,

the stripline field is given by

$$\mathbf{B}_{DC}(x_0, y) = \frac{\mu_0 I_{DC}}{2\pi w} \left(\frac{1}{2} \ln \left(\frac{x_0^2 + (y + w/2)^2}{x_0^2 + (y - w/2)^2} \right) \hat{\mathbf{x}} + \arctan \left(\frac{wx_0}{x_0^2 + y^2 - (w/2)^2} \right) \hat{\mathbf{y}} \right) \quad (1)$$

To facilitate the analysis of the ESR spectra, we also applied a small bias field \mathbf{B}_0 to increase the splitting of the 8 ESR transitions of the 4 NV families. From the total field $\mathbf{B} = \mathbf{B}_0 + \mathbf{B}_{DC}$, we calculate the ESR frequencies for the 4 NV families by diagonalizing the NV spin Hamiltonian $H = DS_z^2 + \gamma(B_{\parallel}S_z + B_{\perp}S_x)$, where B_{\parallel} is the projection of \mathbf{B} onto the NV axis and $B_{\perp} = \sqrt{B^2 - B_{\parallel}^2}$. From the fit to this model (Fig. S1 C), we extract $\mathbf{B}_0 = (0.461(3), 3.568(3), 0.626(3))$ mT, $D = 2.872(1)$ GHz and $x_0 = 1.8(2)$ μm . For the sample in Fig. 4 we used an alternative, optical method to determine the distance, focusing the excitation laser first on the YIG surface and then on the NV layer, reading off the change in the position of the microscope objective from its closed-loop piezo-controller, measuring $x_{0,\text{Sample2}} = 1.0(3)$ μm .

Section S2: Determination of M_s and thickness of YIG with VNA measurements

The YIG saturation magnetization M_s and thickness d are important parameters for analyzing the spin-wave dispersion. Here we describe the extraction of these parameters using vector network analyzer (VNA) measurements.

We flip-chip a YIG chip on the central conductor of a coplanar waveguide (CPW) and use a VNA to measure the microwave transmission S_{21} through the CPW as a function of a magnetic field B_0 applied in-plane and parallel to the central conductor of the CPW (Fig. S2 A). When the frequency matches the YIG FMR, energy is absorbed and S_{21} decreases. We extract $M_s = 1.42(1) \cdot 10^5$ A/m by fitting the data with the Kittel equation $\omega = \gamma\sqrt{B_0(B_0 + \mu_0 M_s)}$.

We determine the thickness of the YIG chip from the frequency of the first perpendicular standing spin-wave mode (PSSW) (43). To extract the frequency of the first PSSW, we measure the spin-wave mediated transmission of microwaves between two striplines using the VNA (Fig.

S2 B-C). The PSSW manifests as a small dip in the transmission (indicated by the dashed black line in Fig. S2 B and the black arrow in Fig. S2 D). To extract the thickness d , we calculate the PSSW frequency at each field for fixed M_s and different values of the thickness using (44). The best match is reached for $d = 245(5)$ nm.

Section S3: Effect of the spin wave stray field on the NV spins

In this section we derive the NV Rabi frequency due to the stray fields from spin waves excited in the YIG by a stripline carrying an oscillating current. In section S3.2 we present the magnetization profile excited by the stripline magnetic field, based on the spin susceptibility of the YIG. In section S3.3 we provide the dipolar field generated by the magnetization oscillations at the NV centers and determine their Rabi frequency by evaluating the efficiency of the field in driving the NV spins, including the chirality of the spin-wave field. In section S3.4, we extend the results obtained to the case of two adjacent striplines and calculate the interference pattern. Our theoretical framework captures and explains several effects visible in the data, such as the spin wave focussing and caustics beams, as well as the interference fringes.

S3.1 Model and parameters

We use the reference frame depicted in Fig. 1 of the main text. Additionally, the length, width and thickness of the stripline are referred to as l , w and δ , respectively, the thickness of the yttrium iron garnet (YIG) film is d , and the NV-YIG distance is x_0 . The static magnetic field B_0 is always applied at a $\phi=35^\circ$ angle with respect to the sample plane and parallel to the striplines. Because B_0 in the experiments of Figs. 2-4 does not exceed 27 mT, which is much smaller than the YIG saturation magnetization $\mu_0 M_s \approx 178$ mT, the static magnetization of the film only tilts out of plane by a small angle $B_0 \sin \phi / (\mu_0 M_s) \lesssim 5^\circ$. We therefore disregard the out-of-plane component of the static magnetization and magnetic field B_0 in the calculations. We use the parameters $w = 2.5 \mu\text{m}$, $\delta = 200$ nm, $l = 88 \mu\text{m}$, $d = 245$ nm and $x_0 = 1 \mu\text{m}$. The

striplines in Fig. 4 E-F of the main text are 110 μm apart and driven with a phase difference of π .

S3.2 Magnetization excited by a microwave stripline of finite length

S3.2.1 Stripline magnetic field

Two striplines $i = \{1, 2\}$ carrying a current density $\mathbf{J}_i(\mathbf{r}, \omega)$ with frequency ω generate the vector potentials (45)

$$\mathbf{A}_i(\mathbf{r}, \omega) = \frac{\mu_0}{4\pi} \int d\mathbf{r}' \mathbf{J}_i(\mathbf{r}', \omega) \frac{e^{ik|\mathbf{r}-\mathbf{r}'|}}{|\mathbf{r}-\mathbf{r}'|}, \quad (2)$$

parallel to the direction of the current (the z -direction). μ_0 is the vacuum permeability and $k = \omega/c$. Substituting the Weyl identity (46),

$$\frac{e^{ik\sqrt{(x-x')^2+(y-y')^2+(z-z')^2}}}{\sqrt{(x-x')^2+(y-y')^2+(z-z')^2}} = \frac{i}{2\pi} \int dk_y dk_z \frac{e^{ik_x|x-x'|+ik_y(y-y')+ik_z(z-z')}}{k_x}, \quad (3)$$

where $k = \sqrt{k_x^2 + k_y^2 + k_z^2}$ (and hence $k_x = \sqrt{k^2 - k_y^2 - k_z^2}$), the Fourier components of the magnetic field $\mu_0(H_x, H_y)^{(i)} = (\partial A_z/\partial y, -\partial A_z/\partial x)^{(i)}$ in reciprocal space are

$$H_x^{(i)}(x; k_y, k_z) = 2iJ_i(\omega) \frac{e^{-ik_x x} e^{ik_x \delta} - 1}{k_x} \sin\left(k_y \frac{w}{2}\right) \frac{\sin(k_z l_i/2)}{k_z} e^{-ik_z z_i}, \quad (4)$$

$$H_y^{(i)}(x; k_y, k_z) = 2iJ_i(\omega) \frac{e^{-ik_x x} e^{ik_x \delta} - 1}{k_x} \sin\left(k_y \frac{w}{2}\right) \frac{\sin(k_z l_i/2)}{k_z} e^{-ik_z z_i}, \quad (5)$$

where $k_x = \sqrt{(\omega/c)^2 - k_y^2 - k_z^2}$, z_i are the z -coordinates of the centers of the striplines and the total current is given by $J_i w \delta$. The generated magnetic field is perpendicular to the stripline axis, i.e. $H_z = 0$, and $k_x H_x(x; k_y, k_z) = k_y H_y(x; k_y, k_z)$. Since $l \gg w$, the magnetic field oscillates as function of k_z with a short period of $4\pi/l$, while it oscillates with k_y with a much longer period of $4\pi/w$ (Fig. S3 A). For a frequency $\omega/(2\pi) \sim 2$ GHz, $k_0 \equiv \omega/c = 4.19$ rad/m with characteristic wavelength $\lambda_0 = 2\pi/k_0 = 0.15$ m. The wavelength of the excited spin waves is much smaller than this scale, indicating that $\sqrt{k_y^2 + k_z^2} \gg \omega/c$. Thus, $k_x \rightarrow i\sqrt{k_y^2 + k_z^2} = i\kappa$.

With $\kappa\delta \ll 1$:

$$\begin{aligned} H_x^{(i)}(x; k_y, k_z) &= -2iJ_i(\omega)e^{\kappa x}\frac{e^{-\kappa\delta} - 1}{\kappa^2} \sin\left(k_y\frac{w}{2}\right) \frac{\sin(k_z l_i/2)}{k_z} e^{-ik_z z_i}, \\ H_y^{(i)}(x; k_y, k_z) &= 2J_i(\omega)e^{\kappa x}\frac{e^{-\kappa\delta} - 1}{\kappa k_y} \sin\left(k_y\frac{w}{2}\right) \frac{\sin(k_z l_i/2)}{k_z} e^{-ik_z z_i}. \end{aligned} \quad (6)$$

The magnetic field distribution in \mathbf{k} -space is plotted in Fig. S3 A for the sample dimensions specified above, emphasizing the fast k_z oscillations. A microwave excitation with field components $h_x = \pm ih_y$ is circularly polarized. The relation

$$H_x(x; k_y, k_z) = -i(k_y/\kappa)H_y(x; k_y, k_z). \quad (7)$$

implies that when $|k_y| \ll |k_z|$, $|H_x| \ll |H_y|$, so the radiation is nearly linearly-polarized along the \hat{y} -direction (in momentum space). On the other hand, when $|k_y| \gg |k_z|$, $H_x(x; k_y, k_z) \rightarrow -i\text{sgn}(k_y)H_y(x; k_y, k_z)$ is nearly right- (left-) circularly polarized for positive (negative) k_y . The polarization-momentum locking of the stripline magnetic field is responsible for the chiral pumping of circularly-polarized spin waves (24,35,47).

S3.2.2 Excited magnetization

The stripline magnetic field excites spin waves in the YIG film. In the mixed position and momentum space, the dynamic magnetization $\mathbf{M}(x, \mathbf{k}, \omega)$ reads in linear response (24,35,47)

$$M_\alpha(x, \mathbf{k}, \omega) = \frac{1}{d} \int_{-d}^0 dx' \chi_{\alpha\beta}(x, x', \mathbf{k}, \omega) H_\beta(x', \mathbf{k}, \omega) \quad (8)$$

where we sum over repeated Cartesian indices $\alpha, \beta = \{x, y, z\}$. γ is the electron gyromagnetic ratio and the spin susceptibility reads (24)

$$\chi_{\alpha\beta}(x, x', \mathbf{k}, \omega) = -\gamma\mu_0 M_s m_\alpha^{\mathbf{k}}(x) m_\beta^{\mathbf{k}*}(x') \frac{1}{\omega - \omega_{\mathbf{k}} + i\Gamma_{\mathbf{k}}}. \quad (9)$$

Here, $m_\alpha^{\mathbf{k}}(x)$ characterize the ellipticity of the magnetization precession associated with the spin waves (see Eq. (11) and Eq. (13)), and $\Gamma_{\mathbf{k}} = 2\alpha_G\omega_{\mathbf{k}}$ is the Gilbert damping of the spin waves with frequency $\omega_{\mathbf{k}}$.

For the parameters of our experiments, the spin waves are in the dipolar-exchange regime with strongly anisotropic dispersion. For the long wavelengths considered here, the magnetization is homogeneous across the film thickness, which allows for an analytical treatment. The spin-wave dispersion for free magnetization boundary conditions reads (24,35,47)

$$\omega_{\mathbf{k}} = \gamma\mu_0 M_s \sqrt{[\Omega_H + \alpha_{\text{ex}}k^2 + 1 - f(|k_y|)] [\Omega_H + \alpha_{\text{ex}}k^2 + (k_y^2/k^2)f(|k_y|)]}, \quad (10)$$

where α_{ex} is the exchange stiffness, $\Omega_H \equiv B_0 \cos(\phi)/\mu_0 M_s$, and

$$f(|k_y|) = 1 - \frac{1}{|k_y|d} + \frac{1}{|k_y|d} \exp(-|k_y|d).$$

At long wavelengths, m_x and m_y are homogeneous across the film thickness and given by

$$m_x = \sqrt{\frac{\mathcal{D} + 1}{\mathcal{D} - 1}}, \quad m_y = i\sqrt{\frac{\mathcal{D} - 1}{\mathcal{D} + 1}}, \quad (11)$$

with

$$\mathcal{D} = \frac{1/2 - (1/2)(1 + k_y^2/k^2)f(|k_y|)}{\omega_{\mathbf{k}}/(\mu_0\gamma M_s) - (\Omega_H + \alpha_{\text{ex}}k_y^2 + 1/2) + (1/2)(1 - k_y^2/k^2)f(|k_y|)}. \quad (12)$$

We define the ellipticity parameter

$$\eta = \frac{|m_x|}{|m_y|} = \frac{\mathcal{D} + 1}{\mathcal{D} - 1}. \quad (13)$$

In the dipolar regime, the spin waves precess elliptically. When $\mathbf{k} \rightarrow 0$, $f(|k_y|) \rightarrow 0$, $\omega_{\mathbf{k}} \rightarrow \mu_0\gamma M_s \sqrt{\Omega_H(\Omega_H + 1)}$ (corresponding to the FMR frequency), $\mathcal{D} \rightarrow -1 - 2\Omega_H - 2\sqrt{\Omega_H(\Omega_H + 1)}$. When $\Omega_H \rightarrow 0$ with a small static magnetic field, $\mathcal{D} \rightarrow -1 - 2\sqrt{\Omega_H}$, $|m_y| \gg |m_x|$, leading to a (nearly) linearly-polarized Kittel mode. When k is large, the exchange interaction dominates and the spin waves are right-circularly polarized.

We plot the calculated excited transverse magnetization amplitude in momentum space in Fig. S3 B-C with parameters similar to those in Fig. 4F of the main text, i.e. $M_s = 1.42 \cdot 10^5$ A/m, $\alpha_G = 1 \times 10^{-4}$, $\omega/2\pi = 2.29$ GHz. The momentum distribution of the resonantly

excited spin waves reflects the hyperboles formed by the cut through the anisotropic spin wave dispersion at the given frequency. The excitation becomes unidirectional when the spin waves are circularly-polarized (24,47), in which case only those with positive values of k_y are excited. Due to the YIG thickness much smaller than the wavelengths considered, this chirality is not the intrinsic one of Damon-Eshbach surface modes, which exist only in much thicker films.

The real part of the inverse Fourier transform of Eq. (8) gives the observable spatiotemporal magnetization

$$\mathbf{M}_\alpha(\boldsymbol{\rho}, t) = \frac{1}{4\pi^2} \iint d\mathbf{k} e^{i\boldsymbol{\rho}\cdot\mathbf{k} - i\omega t} \mathbf{M}_\alpha(x, \mathbf{k}) \quad (14)$$

with $\boldsymbol{\rho} = (y, z)$. Using this equation, we calculate a snapshot of the dynamic magnetization when spin waves are driven by a stripline as in Fig. 4 of the main text (Fig. S4). We observe interference of spin waves with frequency ω . Triangular areas of weak and strong excitation exist at the sides and in front of the stripline, respectively, with a spin wave focus point at the vertex of the latter triangle. These features can be understood from the anisotropy of the spin wave dispersion that leads to a critical opening angle of available spin wave momenta at a given frequency.

S3.3 Dipolar field and Rabi frequency

When the frequency of the magnetic stray field generated by a spin wave matches an NV ESR frequency, it can drive Rabi rotations of the NV spin if it has a circularly polarized component of the correct handedness. Here we describe the spin-wave induced Rabi driving of the NV spins.

S3.3.1 Dipolar field generated by an oscillating magnetization

The magnetic field generated by a magnetization pattern can be calculated using Coulomb's law (45)

$$\mathbf{B}_\beta(\mathbf{r}, t) = \frac{\mu_0}{4\pi} \partial_\beta \partial_\alpha \int d\mathbf{r}' \frac{\mathbf{M}_\alpha(\mathbf{r}', t)}{|\mathbf{r} - \mathbf{r}'|}. \quad (15)$$

By substituting the magnetization from Eq. (14) and using the Coulomb integral

$$\int d\mathbf{r}' \frac{e^{i\mathbf{k}\cdot\boldsymbol{\rho}'} f(x')}{|\mathbf{r}-\mathbf{r}'|} = \frac{2\pi}{k} e^{i\mathbf{k}\cdot\boldsymbol{\rho}} \int dx' e^{-|x-x'|k} f(x'), \quad (16)$$

where $k = |\mathbf{k}|$, we obtain the magnetic field above the film ($x > 0$) (24,35,47)

$$B_{SW,x}(x, \mathbf{k}, t) = \frac{\mu_0}{2} e^{-kx-i\omega t} (1 - e^{-kd}) \left(M_x(\mathbf{k}) - i \frac{k_y}{k} M_y(\mathbf{k}) \right), \quad (17)$$

with $B_{SW,y}(\mathbf{k}) = -i(k_y/k)B_{SW,x}(\mathbf{k})$, and $B_{SW,z}(\mathbf{k}) = -i(k_z/k)B_{SW,x}(\mathbf{k})$. Thus, when $|k_z| \ll |k_y|$, $B_{SW,y}(\mathbf{k}) = -i\text{sign}(k_y)B_{SW,x}(\mathbf{k})$, i.e. the polarization and momentum are locked. $B_{SW,(x,y)}$ vanishes for negative k_y when the spin waves are right circularly-polarized since $M_x(\mathbf{k}) - iM_y(\mathbf{k})k_y/k \rightarrow 0$ (24,47). The right-forward dipolar field is left-circularly polarized.

In real space, the stray field generated by the spin wave is given by the real part of the inverse Fourier transform

$$\mathbf{B}_{SW}(x, \boldsymbol{\rho}, t) = \frac{1}{4\pi^2} \iint e^{i\boldsymbol{\rho}\cdot\mathbf{k}} \mathbf{B}_{SW}(x, \mathbf{k}, t) d\mathbf{k}. \quad (18)$$

A snapshot of the spin-wave stray field at a distance x_0 above the film is plotted in Fig. S5. Since the distance to the film is much smaller than the relevant wavelengths, the interference pattern of the spin waves is well resolved. We note that $|B_{SW,z}| \ll |B_{SW,x}|, |B_{SW,y}|$ because the excited spin waves propagate almost perpendicular to the stripline. The strong chirality (unidirectionality) is caused by both the stripline magnetic field (see in Fig. S3) and the stray field from the spin waves (24,35,47). All Cartesian vector components exert a torque on the NV center spin, which is oriented at an angle to the film. The dipolar field shows a focal point with large amplitude, which can be controlled by tuning the magnetic field and stripline frequency, which could be interesting for spintronic applications.

The field of a spin wave that is characterized by $|k_z| \ll |k_y|$ (therefore $\mathbf{k} \perp \mathbf{M}$, corresponding to a Damon-Eshbach geometry and an effectively one-dimensional configuration) is given by ($x > 0$)

$$\mathbf{B}_{SW}(x, \mathbf{k}, t) = -\frac{\mu_0}{2} e^{-kx-i\omega t} (1 - e^{-kd}) M_y(\mathbf{k}) (1 + \text{sign}(k_y)\eta) (\hat{\mathbf{y}} + i\text{sign}(k_y)\hat{\mathbf{x}}), \quad (19)$$

where we used $M_x = -i\eta M_y$. To arrive at the equations given in the main text, we calculate the field of a traveling spin wave given by the real part of $\mathbf{m}_\perp = m_\perp^0 e^{i(k_0 y - \omega t)}(\hat{\mathbf{y}} - i\eta\hat{\mathbf{x}})$. The Fourier transform of the y -component is

$$M_y(k_y) = m_\perp^0 2\pi\delta(k_y - k_0). \quad (20)$$

Substituting into Eq. (19) and taking the inverse Fourier transform, we get Eq. (2) of the main text

$$\mathbf{B}_{\text{SW}}(y) = -\text{Re}\left[\frac{\mu_0 m_\perp^0}{2} e^{-|k_0|x_0} e^{i(k_0 y - \omega t)} (1 - e^{-|k_0|d}) (1 + \text{sign}(k_0)\eta) (\hat{\mathbf{y}} + i\text{sign}(k_0)\hat{\mathbf{x}})\right] \quad (21)$$

$$= -\text{Re}[B_{\text{SW}}^0 e^{i(k_0 y - \omega t)} (\hat{\mathbf{y}} + i\text{sign}(k_0)\hat{\mathbf{x}})] \quad (22)$$

S3.3.2 Calculation of the Rabi frequency

The dynamic magnetic field generated by the spin waves can induce transitions between the spin states of the NV center when its frequency matches an NV ESR frequency as described by the NV spin Hamiltonian. We write the dynamic part of the magnetic field as

$$\mathbf{B}_{\text{SW}}(y) = \text{Re}[(B_x \hat{\mathbf{x}} + B_y \hat{\mathbf{y}} + B_z \hat{\mathbf{z}}) e^{-i\omega t}] \quad (23)$$

In the local coordinates of the NV center, with the z' -direction along the applied static magnetic field (therefore along the NV axis), the field amplitudes becomes

$$B_{x'} = B_x \cos \phi - B_z \sin \phi, \quad (24)$$

$$B_{y'} = B_y, \quad (25)$$

$$B_{z'} = B_z \cos \phi + B_x \sin \phi. \quad (26)$$

The Hamiltonian describing the NV spin dynamics is given by

$$H_{\text{NV}} = DS_z^2 + \gamma \mathbf{B}' \cdot \mathbf{S} \quad (27)$$

where $\mathbf{S} = (S_x, S_y, S_z)$ are the Pauli matrices for a spin 1 and $D/2\pi = 2.87$ GHz is the zero-field frequency. The two magnetic-dipole allowed transitions between the $m_s = 0$ and the $m_s = \pm 1$ states are driven by magnetic fields of opposite handedness. When the magnetic-field frequency ω matches one of the NV ESR frequencies $D \pm \gamma B_0$, the NV spin will Rabi oscillate between the corresponding $m_s = 0$ and $m_s = \pm 1$ states with a Rabi frequency given by

$$\omega_R^\pm = \frac{\gamma}{\sqrt{2}} |B_{x'} \pm iB_{y'}|. \quad (28)$$

We use Eq. (28) to calculate the spin-wave induced Rabi frequency caused by the spatial magnetization profile shown in Fig. S4. The Rabi frequency closely resembles the spatial magnetization profile, including the presence of caustic beams and a focal point (Fig. S6).

When the NV ω_- transition is driven by a resonant Damon-Eshbach spin wave with $k_0 > 0$, we get

$$\omega_R^- = \sqrt{2}\gamma B_{\text{SW}}^0 \cos^2 \frac{\phi}{2}. \quad (29)$$

If the NV spin is also driven by a magnetic field that is given by $\text{Re}[\mathbf{B}_{\text{REF}} e^{-i\omega t}]$, we get

$$\omega_R^- = \frac{\gamma}{\sqrt{2}} \left| 2B_{\text{SW}}^0 e^{ik_0 y} \cos^2 \frac{\phi}{2} + B_{\text{REF},x'} - iB_{\text{REF},y'} \right|. \quad (30)$$

from which follows Eq. 3 of the main text. Including a damping parameter into Eq. (30), we fit the data of Fig. 2B of the main text, from which we extract the spin-wave amplitude m_\perp^0 (using the ellipticity parameter calculated with Eq. (13)) and the spin-wave damping:

$$\omega_R^- = \frac{\gamma}{\sqrt{2}} \left| 2B_{\text{SW}}^0 e^{ik_0 y - y/y_0} \cos^2 \frac{\phi}{2} + e^{i\theta} B_{\text{REF}} \right|. \quad (31)$$

Here, y_0 is the spin-wave decay length from which the Gilbert damping parameter is extracted using $y_0 = v_g/(2\omega\alpha_G)$, with v_g the group velocity, leading to $\alpha_G = 1.2(1) \cdot 10^{-4}$. The main contribution to the uncertainty is caused by the uncertainty in the NV-YIG distance, which we measured to be $1.8(2) \mu\text{m}$ (see section S1) at the location of the stripline and which increases

by about $0.4 \mu\text{m}/\text{mm}$ as estimated from the optical interference fringes visible in Fig. 1B of the main text (the distance change between two fringes is given by $\lambda_0/2$, with λ_0 the wavelength of the light in air). Using Eq. (31), we also fitted the data shown in Fig. 3B of the main text, with B_{REF} given by Eq. (1).

S3.4 Effect of magnetic field misalignment on the observed spin-wave patterns

To explain the asymmetry along \hat{z} of the observed spin-wave patterns in Fig. 4, we repeat the calculation of Fig. 4C with the introduction of a 5° misalignment between the static field and the stripline (Fig. S7). The tilt is from the \hat{z} toward the $-\hat{y}$ axis.

S3.5 Influence of the spin-wave propagation direction on the field profile

As previously explained (S3.3.2, Eq. (28)), right(left)-propagating spin waves generate a circularly-polarized field with handedness that drives the ω_- (ω_+) transition. Moreover, for perfectly circular polarization, the right(left)-propagating waves only generate a field above (below) the film, which can be simply explained by cancellation of the field contributions of neighbouring spins (Fig. S8). For elliptical polarization, the field suppression is not complete.

S3.6 Interference between spin waves generated by two adjacent striplines

Finally, we calculate the interference pattern generated by two striplines on the YIG film, with centers separated by $200 \mu\text{m}$. With $l_1 = 100 \mu\text{m}$ and $l_2 = -100 \mu\text{m}$ in Eq. (6) and considering the π phase difference between the two striplines

$$H_x(x; k_y, k_z) = -2iJ(\omega)e^{\kappa x} \frac{e^{-\kappa\delta} - 1}{\kappa^2} \sin\left(k_y \frac{w}{2}\right) \frac{\sin(k_z l/2)}{k_z} (e^{-ik_z z_1} - e^{-ik_z z_2}), \quad (32)$$

$$H_y(x; k_y, k_z) = 2J(\omega)e^{\kappa x} \frac{e^{-\kappa\delta} - 1}{\kappa k_y} \sin\left(k_y \frac{w}{2}\right) \frac{\sin(k_z l/2)}{k_z} (e^{-ik_z z_1} - e^{-ik_z z_2}). \quad (33)$$

By substitution into Eqs. (8) and (17), we obtain the Rabi frequencies of the NV center in Figure S9. The spin-wave interference is clearly reflected in the Rabi frequency.

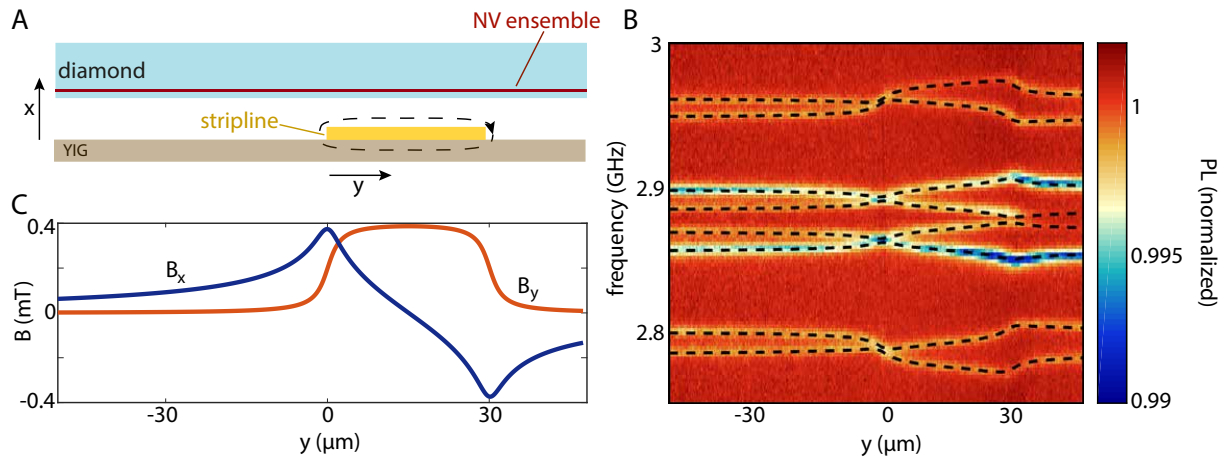


Fig. S1. Determination of the YIG-NV distance. (A) Idea of the measurement. The diamond is located at a height x above the current-carrying stripline fabricated on the YIG. ESR spectra are measured along a line perpendicular to the stripline. The current in the stripline generates a magnetic field (dashed black line), causing a shift of the NV ESR frequencies. (B) NV ESR spectra measured along a line oriented perpendicularly to the stripline (which is located between $y=0$ and $y=30 \mu\text{m}$). The eight dips in the photoluminescence (PL) are caused by the ESR transitions of the four NV families having different orientations in the diamond crystal lattice. (C) Stripline magnetic field in the NV layer corresponding to the values extracted from the fit.

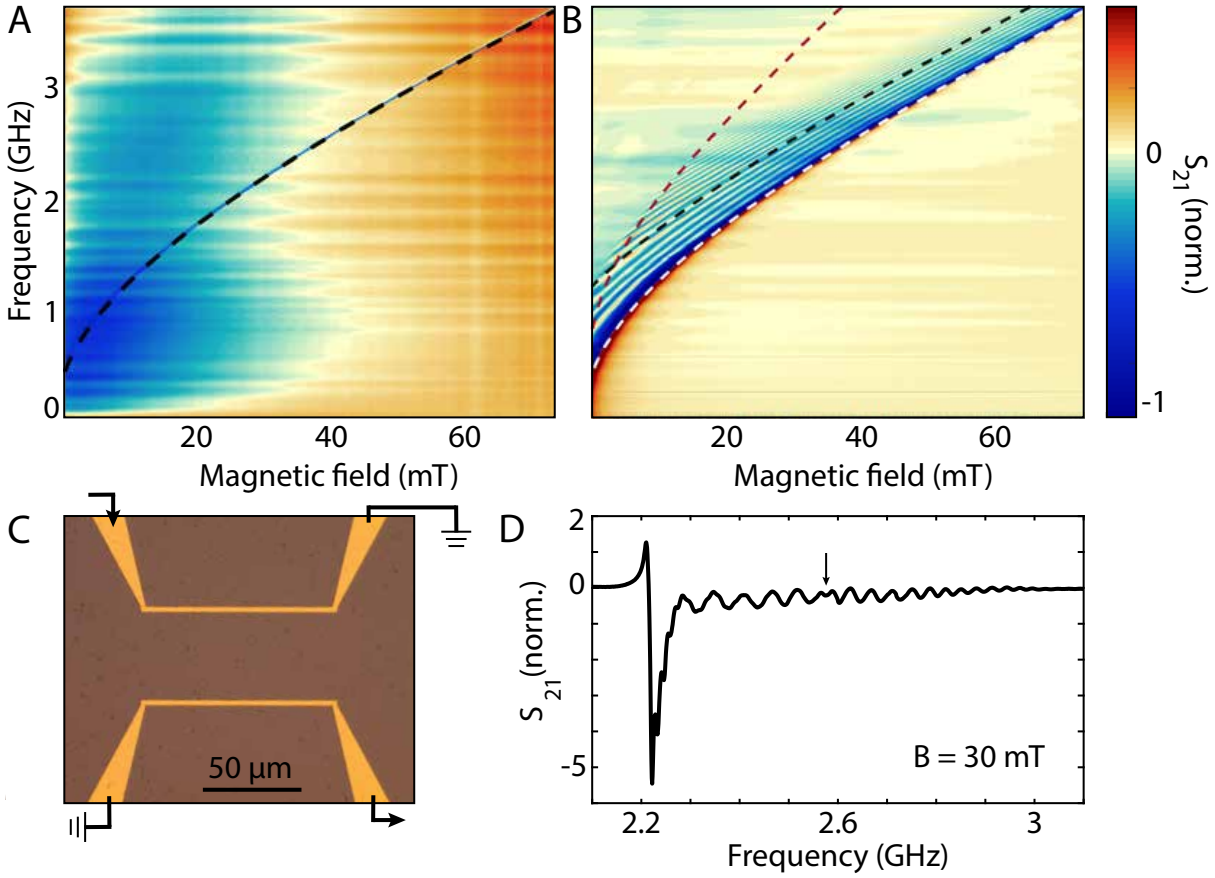


Fig. S2. VNA-FMR detection of spin waves to determine M_s and thickness of the YIG chip. (A) Transmission $S_{21}(B, \omega)$ through the central conductor of a CPW on top of which a YIG chip is placed. The absorption of YIG at the FMR (dark blue line in the data) is extremely sharp (FWHM < 10 MHz). The dashed black line is calculated using the extracted value of $M_s = 1.42 \cdot 10^5$ A/m. (B) $S_{21}(B, \omega)$ mediated by spin waves across the device shown in (C). The white and black dashed lines are the calculated frequencies of the FMR and 1st-order PSSW, respectively. The red dashed line indicates a frequency that is twice that of the calculated band minimum. Above this frequency, three-magnon scattering becomes allowed, which may contribute to the observed vanishing of the spin-wave mediated transmission above this frequency. (C) Device used to obtain the measurement in (B). The two gold striplines fabricated on YIG and connected to the input and output of the VNA as indicated by the arrows. Stripline width = 2.5 μm , thickness = 200 nm. (D) Vertical linecut of (B) at 30 mT, showing the FMR absorption dip followed by several oscillations and the PSSW, indicated by the black arrow.

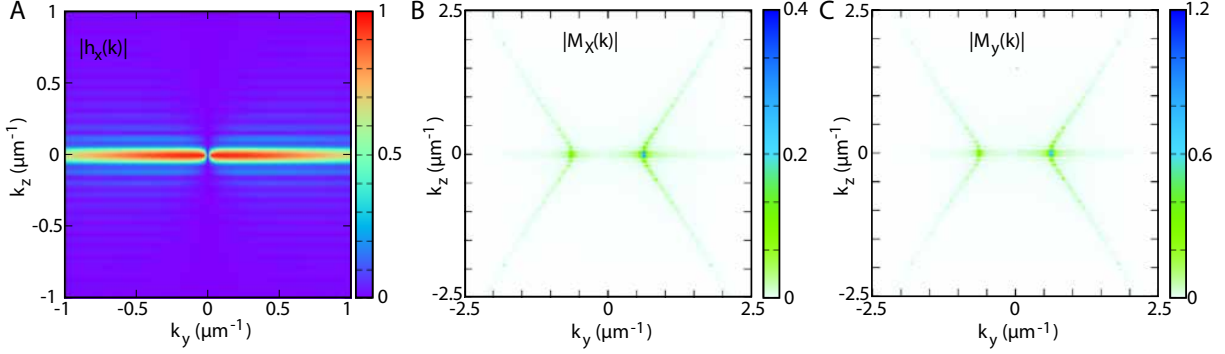


Fig. S3. Drive field and excited magnetization in reciprocal space. (A) x -component of the magnetic field generated by the stripline in momentum space. (B)-(C) Resulting transverse magnetization amplitude, for $\alpha_G = 1 \times 10^{-4}$, $\omega = 2.29$ GHz, $\mu_0 M_s = 0.178$ T, and applied magnetic field $B_0 = 20$ mT. Note the different scales used for plotting $|M_x|$ and $|M_y|$.

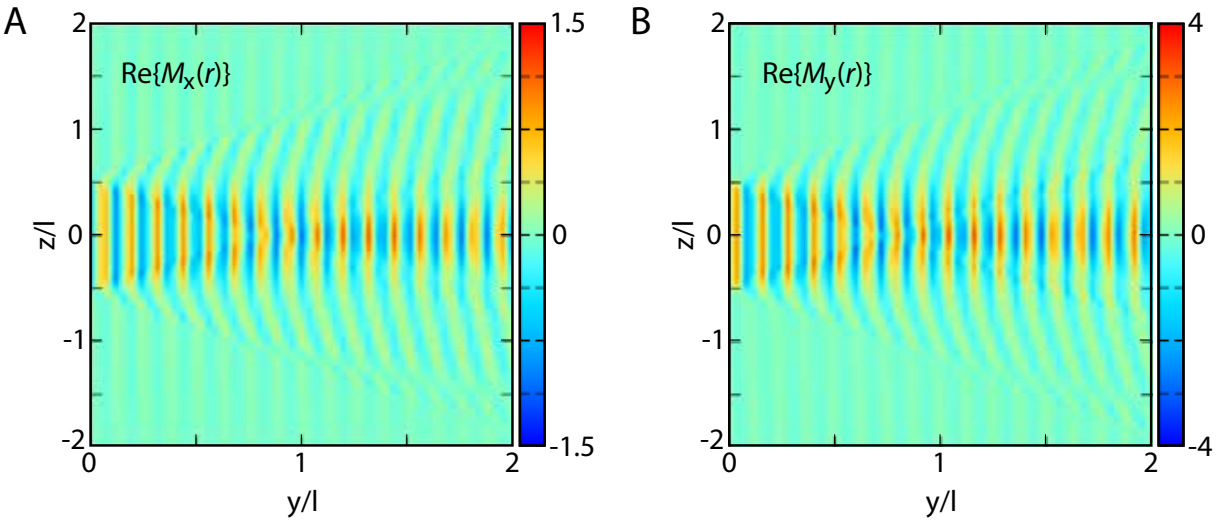


Fig. S4. Spatial profile of the excited magnetization. Spatial profile of the out-of-plane (A) and in-plane (B) of the transverse magnetization oscillations excited by a single stripline, located at $y = 0$ between $z/l = -0.5$ and $z/l = +0.5$.

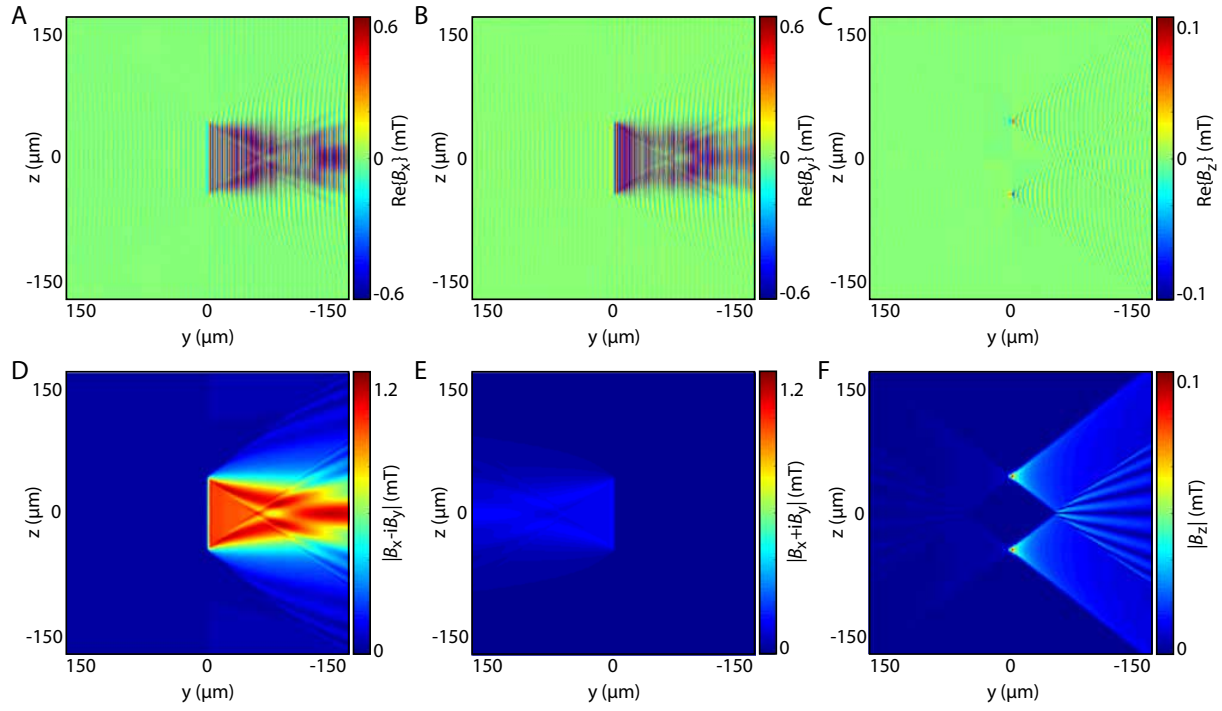


Fig. S5. Spatial profile of the dipolar field generated by spin waves. Snapshot of the stray field in real space at $t = 0$ for a microwave driving with a frequency $\omega = 2.29$ GHz and a stripline current of 0.7 mA at a distance x_0 above the film. The stripline is located at $y = 0$, $z \in [-40, 40]\mu\text{m}$. The damping coefficient is $\alpha_G = 10^{-4}$.

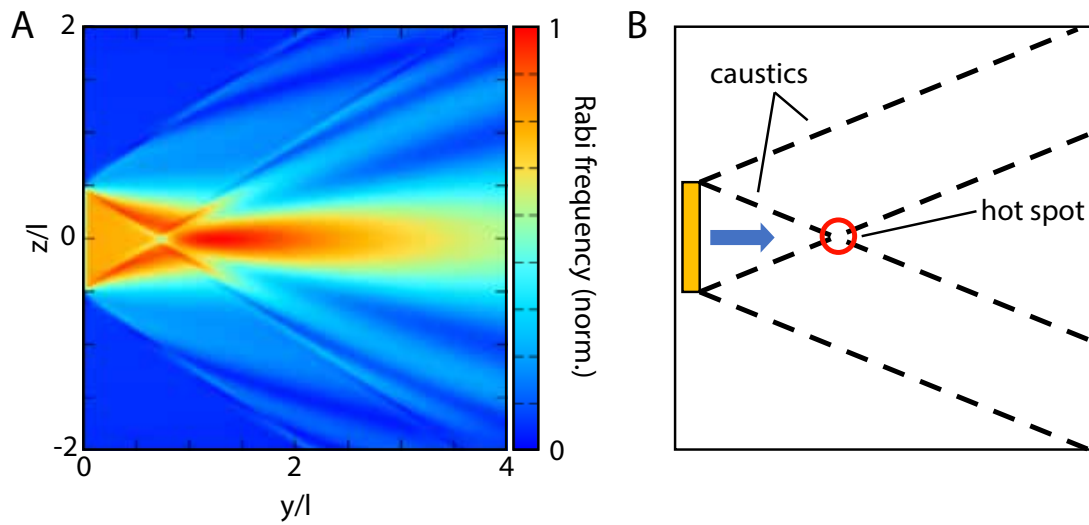


Fig. S6. Calculated spatial map of the Rabi frequency for a single stripline. (A) Rabi frequency calculated from the dipolar field without the (small) direct contribution from the stripline at $y = 0$ and $z/l \in [-0.5, 0.5]$. (B) Schematics indicating the emergence of caustic spin-wave beams and the "hot spot" where energy gets focussed.

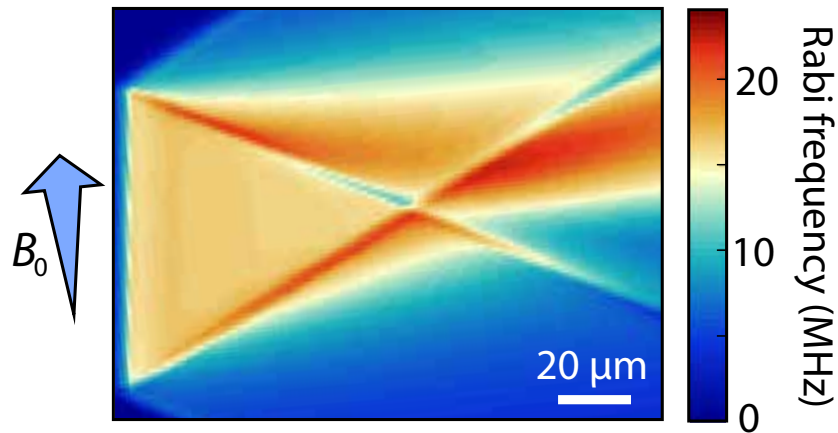


Fig. S7. Effect of a small angle between the stripline and the in-plane component of the static field B_0 . Calculated spatial map of the Rabi frequency when the in-plane projection of the static field (B_0) is oriented at a 5° angle from the stripline.

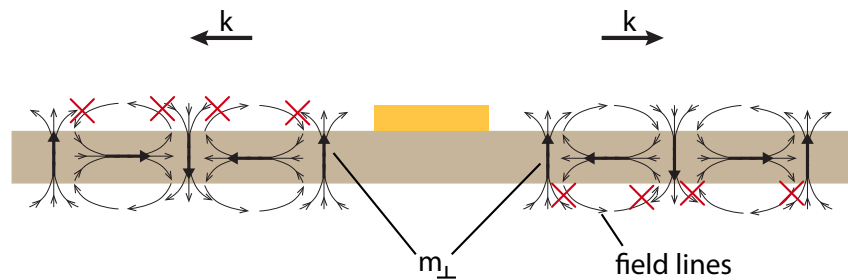


Fig. S8. Magnetic field generated by spin waves propagating to the left and right. The magnetic stray field generated by a spin wave is the sum of the fields generated by the individual precessing spins in the magnet. The phases of the spin waves traveling to the right interfere constructively/destructively above/below the film, and vice versa for spin waves traveling to the left.

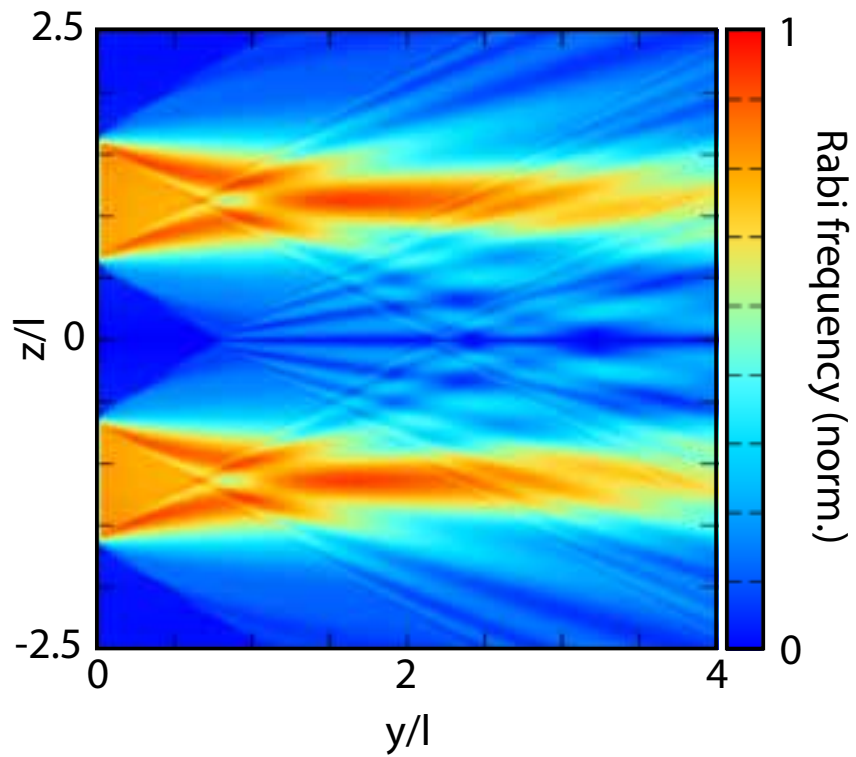


Fig. S9. Calculated spatial map of the Rabi frequency induced by two adjacent striplines. We observe interference of spin waves generated by two striplines located at $y = 0$ for $z \in \pm[0.5, 1.5]$.

REFERENCES AND NOTES

1. V. V. Kruglyak, S. O. Demokritov, D. Grundler, Magnonics. *J. Phys. D Appl. Phys.* **43**, 264001 (2010).
2. A. V. Chumak, V. I. Vasyuchka, A. A. Serga, B. Hillebrands, Magnon spintronics. *Nat. Phys.* **11**, 453–461 (2015).
3. K. Vogt, F. Y. Fradin, J. E. Pearson, T. Sebastian, S. D. Bader, B. Hillebrands, A. Hoffmann, H. Schultheiss, Realization of a spin-wave multiplexer. *Nat. Commun.* **5**, 3727 (2014).
4. A. V. Chumak, A. A. Serga, B. Hillebrands, Magnon transistor for all-magnon data processing. *Nat. Commun.* **5**, 4700 (2014).
5. L. J. Cornelissen, J. Liu, B. J. van Wees, R. A. Duine, Spin-current-controlled modulation of the magnon spin conductance in a three-terminal magnon transistor. *Phys. Rev. Lett.* **120**, 097702 (2018).
6. V. E. Demidov, H. Ulrichs, S. V. Gurevich, S. O. Demokritov, V. S. Tiberkevich, A. N. Slavin, A. Zholud, S. Urazhdin, Synchronization of spin Hall nano-oscillators to external microwave signals. *Nat. Commun.* **5**, 3179 (2014).
7. Q. Wang, P. Pirro, R. Verba, A. Slavin, B. Hillebrands, A. V. Chumak, Reconfigurable nanoscale spin-wave directional coupler. *Sci. Adv.* **4**, e1701517 (2018).
8. T. Warwick, K. Franck, J. B. Kortright, G. Meigs, M. Moronne, S. Myneni, E. Rotenberg, S. Seal, W. F. Steele, H. Ade, A. Garcia, S. Cerasari, J. Denlinger, S. Hayakawa, A. P. Hitchcock, T. Tyliczszak, J. Kikuma, E. G. Rightor, H.-J. Shin, B. P. Tonner, A scanning transmission x-ray microscope for materials science spectromicroscopy at the advanced light source. *Rev. Sci. Instrum.* **69**, 2964–2973 (1998).
9. V. Sluka, T. Schneider, R. A. Gallardo, A. Kákay, M. Weigand, T. Warnatz, R. Mattheis, A. Roldán-Molina, P. Landeros, V. Tiberkevich, A. Slavin, G. Schütz, A. Erbe, A. Deac, J. Lindner, J. Raabe, J. Fassbender, S. Wintz, Emission and propagation of 1D and 2D spin waves with nanoscale wavelengths in anisotropic spin textures. *Nat. Nanotechnol.* **14**, 328–333 (2019).

10. T. Sebastian, K. Schultheiss, B. Obry, B. Hillebrands, H. Schultheiss, Micro-focused Brillouin light scattering: Imaging spin waves at the nanoscale. *Front. Phys.* **3**, 35 (2015).
11. Y. Acremann, C. H. Back, M. Buess, O. Portmann, A. Vaterlaus, D. Pescia, H. Melchior, Imaging precessional motion of the magnetization vector. *Science* **290**, 492–495 (2000).
12. L. Rondin, J.-P. Tetienne, T. Hingant, J.-F. Roch, P. Maletinsky, V. Jacques, Magnetometry with nitrogen-vacancy defects in diamond. *Rep. Prog. Phys.* **77**, 056503 (2014).
13. F. Casola, T. van der Sar, A. Yacoby, Probing condensed matter physics with magnetometry based on nitrogen-vacancy centres in diamond. *Nat. Rev. Mater.* **3**, 17088 (2018).
14. I. Gross, W. Akhtar, V. Garcia, L. J. Martínez, S. Chouaieb, K. Garcia, C. Carrétéro, A. Barthélémy, P. Appel, P. Maletinsky, J.-V. Kim, J. Y. Chauleau, N. Jaouen, M. Viret, M. Bibes, S. Fusil, V. Jacques, Real-space imaging of non-collinear antiferromagnetic order with a single-spin magnetometer. *Nature* **549**, 252–256 (2017).
15. L. Rondin, J.-P. Tetienne, S. Rohart, A. Thiaville, T. Hingant, P. Spinicelli, J.-F. Roch, V. Jacques, Stray-field imaging of magnetic vortices with a single diamond spin. *Nat. Commun.* **4**, 2279 (2013).
16. Y. Dovzhenko, F. Casola, S. Schlotter, T. X. Zhou, F. Büttner, R. L. Walsworth, G. S. D. Beach, A. Yacoby, Magnetostatic twists in room-temperature skyrmions explored by nitrogen-vacancy center spin texture reconstruction. *Nat. Commun.* **9**, 2712 (2018).
17. T. van der Sar, F. Casola, R. Walsworth, A. Yacoby, Nanometre-scale probing of spin waves using single-electron spins. *Nat. Commun.* **6**, 7886 (2015).
18. C. Du, T. van der Sar, T. X. Zhou, P. Upadhyaya, F. Casola, H. Zhang, M. C. Onbasli, C. A. Ross, R. L. Walsworth, Y. Tserkovnyak, A. Yacoby, Control and local measurement of the spin chemical potential in a magnetic insulator. *Science* **357**, 195–198 (2017).
19. P. Andrich, C. F. de las Casas, X. Liu, H. L. Bretscher, J. R. Berman, F. J. Heremans, P. F. Nealey, D. D. Awschalom, Long-range spin wave mediated control of defect qubits in nanodiamonds. *npj Quantum Inf.* **3**, 28 (2017).

20. D. Kikuchi, D. Prananto, K. Hayashi, A. Laraoui, N. Mizuochi, M. Hatano, E. Saitoh, Y. Kim, C. A. Meriles, T. An, Long-distance excitation of nitrogen-vacancy centers in diamond via surface spin waves. *Appl. Phys. Express* **10**, 103004 (2017).
21. C. S. Wolfe, V. P. Bhallamudi, H. L. Wang, C. H. Du, S. Manuilov, R. M. Teeling-Smith, A. J. Berger, R. Adur, F. Y. Yang, P. C. Hammel, Off-resonant manipulation of spins in diamond via precessing magnetization of a proximal ferromagnet. *Phys. Rev. B* **89**, 180406 (2014).
22. L. Thiel, Z. Wang, M. A. Tschudin, D. Rohner, I. Gutiérrez-Lezama, N. Ubrig, M. Gibertini, E. Giannini, A. F. Morpurgo, P. Maletinsky, Probing magnetism in 2D materials at the nanoscale with single-spin microscopy. *Science* **364**, 973–976 (2019).
23. A. A. Serga, A. V. Chumak, B. Hillebrands, YIG magnonics. *J. Phys. D Appl. Phys.* **43**, 264002 (2010).
24. T. Yu, Y. M. Blanter, G. E. W. Bauer, Chiral pumping of spin waves. *Phys. Rev. Lett.* **123**, 247202 (2019).
25. C. Dubs, O. Surzhenko, R. Linke, A. Danilewsky, U. Brückner, J. Dellith, Sub-micrometer yttrium iron garnet LPE films with low ferromagnetic resonance losses. *J. Phys. D Appl. Phys.* **50**, 204005 (2017).
26. T. Schneider, A. A. Serga, A. V. Chumak, C. W. Sandweg, S. Trudel, S. Wolff, M. P. Kostylev, V. S. Tiberkevich, A. N. Slavin, B. Hillebrands, Nondiffractive subwavelength wave beams in a medium with externally controlled anisotropy. *Phys. Rev. Lett.* **104**, 197203 (2010).
27. R. Gieniusz, H. Ulrichs, V. D. Bessonov, U. Guzowska, A. I. Stognii, A. Maziewski, Single antidot as a passive way to create caustic spin-wave beams in yttrium iron garnet films. *Appl. Phys. Lett.* **102**, 102409 (2013).
28. M. Mohseni, R. Verba, T. Brächer, Q. Wang, D. A. Bozhko, B. Hillebrands, P. Pirro, Backscattering immunity of dipole-exchange magnetostatic surface spin waves. *Phys. Rev. Lett.* **122**, 197201 (2019).

29. J. R. Eshbach, R. W. Damon, Surface magnetostatic modes and surface spin waves. *Phys. Rev.* **118**, 1208–1210 (1960).
30. J. Chen, T. Yu, C. Liu, T. Liu, M. Madami, K. Shen, J. Zhang, S. Tu, M. S. Alam, K. Xia, M. Wu, G. Gubbiotti, Y. M. Blanter, G. E. W. Bauer, H. Yu, Excitation of unidirectional exchange spin waves by a nanoscale magnetic grating. *Phys. Rev. B.* **100**, 104427 (2019).
31. J.-P. Tetienne, N. Dontschuk, D. A. Broadway, A. Stacey, D. A. Simpson, L. C. L. Hollenberg, Quantum imaging of current flow in graphene. *Sci. Adv.* **3**, e1602429 (2017).
32. T. Rosskopf, A. Dussaux, K. Ohashi, M. Loretz, R. Schirhagl, H. Watanabe, S. Shikata, K. M. Itoh, C. L. Degen, Investigation of surface magnetic noise by shallow spins in diamond. *Phys. Rev. Lett.* **112**, 147602 (2014).
33. C. Wei, A. S. M. Windsor, N. B. Manson, A strongly driven two-level atom revisited: Bloch-Siegert shift versus dynamic Stark splitting. *J. Phys. B At. Mol. Opt. Phys.* **30**, 21 (1997).
34. B. Flebus, Y. Tserkovnyak, Quantum-impurity relaxometry of magnetization dynamics. *Phys. Rev. Lett.* **121**, 187204 (2018).
35. K. Arai, C. Belthangady, H. Zhang, N. Bar-Gill, S. J. Devience, P. Cappellaro, A. Yada, R. L. Walsworth, Fourier magnetic imaging with nanoscale resolution and compressed sensing speed-up using electronic spins in diamond. *Nat. Nanotechnol.* **10**, 859–864 (2015).
36. G. Balasubramanian, I. Y. Chan, R. Kolesov, M. Al-Hmoud, J. Tisler, C. Shin, C. Kim, A. Wojcik, P. R. Hemmer, A. Krueger, T. Hanke, A. Leitenstorfer, R. Bratschitsch, F. Jelezko, J. Wrachtrup, Nanoscale imaging magnetometry with diamond spins under ambient conditions. *Nature* **455**, 648–651 (2008).
37. L. Thiel, D. Rohner, M. Ganzhorn, P. Appel, E. Neu, B. Müller, R. Kleiner, D. Koelle, P. Maletinsky, Quantitative nanoscale vortex imaging using a cryogenic quantum magnetometer. *Nat. Nanotechnol.* **11**, 677–681 (2016).

38. M. Pelliccione, A. Jenkins, P. Ovarthaiyapong, C. Reetz, E. Emmanouilidou, N. Ni, A. C. Bleszynski Jayich, Scanned probe imaging of nanoscale magnetism at cryogenic temperatures with a single-spin quantum sensor. *Nat. Nanotechnol.* **11**, 700–705 (2016).
39. E. Schaefer-Nolte, F. Reinhard, M. Ternes, J. Wrachtrup, K. Kern, A diamond-based scanning probe spin sensor operating at low temperature in ultra-high vacuum. *Rev. Sci. Instrum.* **85**, 013701 (2014).
40. J.-M. Cai, B. Naydenov, R. Pfeiffer, L. P. McGuinness, K. D. Jahnke, F. Jelezko, M. B. Plenio, A. Retzker, Robust dynamical decoupling with concatenated continuous driving. *New J. Phys.* **14**, 113023 (2012).
41. S. E. Lillie, N. Dontschuk, D. A. Broadway, D. L. Creedon, L. C. L. Hollenberg, J.-P. Tetienne, Imaging graphene field-effect transistors on diamond using nitrogen-vacancy microscopy. *Phys. Rev. Appl.* **12**, 024018 (2019).
42. S. Bogdanović, M. S. Z. Liddy, S. B. Van Dam, L. C. Coenen, T. Fink, M. Lončar, R. Hanson, Robust nano-fabrication of an integrated platform for spin control in a tunable microcavity. *APL Photonics* **2**, 126101 (2017).
43. M. A. W. Schoen, J. M. Shaw, H. T. Nembach, M. Weiler, T. J. Silva, Radiative damping in waveguide-based ferromagnetic resonance measured via analysis of perpendicular standing spin waves in sputtered permalloy films. *Phys. Rev. B* **92**, 184417 (2015).
44. B. A. Kalinikos, A. N. Slavin, Theory of dipole-exchange spin wave spectrum for ferromagnetic films with mixed exchange boundary conditions. *J. Phys. C Solid State Phys.* **19**, 7013–7033 (1986).
45. J. D. Jackson, *Classical Electrodynamics* (Wiley, 1998).
46. L. Novotny, B. Hecht, *Principles of Nano-optics* (Cambridge Univ. Press, 2006).
47. T. Yu, C. Liu, H. Yu, Y. M. Blanter, G. E. W. Bauer, Chiral excitation of spin waves in ferromagnetic films by magnetic nanowire gratings. *Phys. Rev. B* **99**, 134424 (2019).